Strengthening Mechanisms in Ultrafine-Grained and Sub-grained High-Purity Aluminum

NAOYA KAMIKAWA, TAISUKE HIROCHI, and TADASHI FURUHARA

This study investigates the effect of grain/sub-grain size, boundary misorientation, and dislocation density on mechanical properties of nanostructured aluminum. A fully recrystallized high-purity aluminum was deformed to different strains from low to ultrahigh strains by a combination of conventional cold rolling and accumulative roll-bonding, followed by annealing for recovery and structural coarsening, to produce sub-grained samples dominated by low-angle boundaries and ultrafine-grained samples dominated by high-angle boundaries. The ultrafine-grained samples showed unusual discontinuous yielding and had a very high strength, which was positively deviated from the extrapolation of the Hall–Petch curve in coarse grains. On the other hand, sub-grained samples showed continuous yielding, and the strength was lower than that of ultrafine-grained samples at the same structural size. It is suggested that in the ultrafine-grained samples, due to lack of dislocation sources in the grains, extremely high stress is required for yielding, which is responsible for the unexpected discontinuous yielding and extra Hall–Petch strengthening. On the other hand, in the sub-grained samples, dislocations in the low-angle dislocation boundaries may act as active dislocation sources, leading to a lower yield stress.

I. INTRODUCTION

IT is well known that yield stress of metals increases inversely proportional to the square root of average grain size, based on the Hall–Petch relationship,[1,2] given as,

$$\sigma_y = \sigma_0 + k d^{-1/2}, \qquad [1]$$

where σ_y is the yield stress, d is the average grain size, and σ_0 and k are constants independent of the grain size. In the last two decades,[3–8] production of ultrafine-grained metals or nanostructured metals, with the average grain size in the micrometer or sub-micrometer scale, has received much attention from both scientific and industrial viewpoints, to significantly increase the strength of metallic materials, as predicted by the Hall–Petch curve in Eq. [1].

However, it has been found, for instance, in pure aluminum,[9–11] pure copper,[12] and ultralow carbon interstitial free (IF) steel[13,14] that the strength of ultrafine-grained metals is positively deviated from the extrapolation of the Hall–Petch curves in coarse grains, resulting in a larger Hall–Petch coefficient k in the ultrafine grains than in coarse grains. This behavior can be termed as "extra Hall–Petch strengthening." It has also been found[9–14] that extra Hall–Petch strengthening is due to the occurrence of unexpected discontinuous yielding accompanied with Lüders deformation in ultrafine-grained metals. Such unexpected discontinuous yielding in ultrafine-grained metals has also been reported in other works, such as pure aluminum,[15] pure copper,[16] pure titanium,[17,18] ultralow carbon IF steel,[19] and high Mn austenitic steel.[20]

To understand the strengthening mechanisms of ultrafine-grained metals, the structure-based strength calculation has been applied in high-purity aluminum produced by accumulative roll-bonding (ARB) and subsequent annealing in a previous work.[10] It has been found from this work that a sum of dislocation strengthening and grain boundary strengthening can reasonably explain the yield stress of as-deformed ultrafine-grained samples as well as fully recrystallized coarse-grained samples, while in well-annealed ultrafine-grained samples produced by high strain deformation and annealing, the experimentally obtained yield stress is much higher than the calculation. These results indicate that strengthening mechanisms are different

NAOYA KAMIKAWA is with the Department of Mechanical Science and Engineering, Graduate School of Science and Technology, Hirosaki University, 3 Bunkyo-cho, Hirosaki, Aomori 036-8561, Japan. Contact e-mail: kamikawa@hirosaki-u.ac.jp TAISUKE HIROCHI is with Tohoku University, 2-1-1 Katahira, Aoba-ku, Sendai, Miyagi 980-8577, Japan and also with Mitsubishi Heavy Industries, Ltd., 1-1-1 Wadasaki-cho, Hyogo-ku, Kobe, Hyogo, 652-8585, Japan. TADASHI FURUHARA is with the Institute for Materials Research, Tohoku University, 2-1-1 Katahira, Aoba-ku, Sendai, Miyagi 980-8577, Japan.

between as-deformed ultrafine-grained samples and well-annealed ultrafine-grained samples. In other words, not only grain size but pre-existing dislocations might play an important role to control the strengthening mechanisms of ultrafine-grained metals.

Concerning the deformation mechanisms in ultrafine-grained metals, it has been suggested[10,21–23] that very high stress is required to activate Frank–Read dislocation sources within ultrafine grains. It has also been suggested that[24–27] in ultrafine-grained metals, grain boundaries would be dominant sources for dislocation activation. If activation of dislocation sources from grain boundaries is a dominant mechanism for yielding in ultrafine-grained metals, grain boundary misorientation or character must affect the strengthening mechanisms of ultrafine-grained metals,[26–35] but systematic experimental evidences are not sufficient to understand the correlation between grain boundary misorientation and macroscopic strength in ultrafine-grained metals.

The present study is therefore motivated to experimentally clarify the effects of pre-existing dislocations, boundary misorientation, as well as grain size on the strengthening mechanisms of ultrafine-grained metals. In particular, this research focuses on the effect of such structural parameters on yielding behavior, Hall–Petch relationship, and strengthening mechanism. A part of the experimental data in this paper has already been reported in a previous conference paper,[33] but this work will present more systematic data and detailed discussion.

II. EXPERIMENTAL

A. *Material*

A high-purity aluminum with a purity of 99.99 mass pct was used to minimize the effect of impurities on mechanical properties. The main impurities were 0.004 pct of Si, 0.001 pct of Cu, and 0.003 pct of Fe. An as-cast ingot with a thickness of approximately 40 mm was cold-rolled down to 10 mm, followed by annealing at 375 °C for 1 hour to obtain a fully recrystallized structure with the average grain size of 162 μm, which was used as a starting material.

B. *Cold Rolling and Accumulative Roll-Bonding (ARB)*

In this study, conventional cold rolling[36–38] was applied to give relatively low strains. The fully recrystallized starting samples were deformed by cold rolling under lubricated condition at room temperature by 50 and 90 pct reductions in thickness, corresponding to an equivalent strain of 0.8 and 2.7, respectively. To realize ultrahigh strains, 90 pct cold-rolled samples were followed by ARB.[39–41] ARB is a kind of severe plastic deformation using rolling process, where cutting, stacking, and roll-bonding can be repeated without changing the thickness of rolled sheet. In this experiment, the 90 pct cold-rolled samples were further deformed by ARB under lubricated condition at room

temperature. After the surface treatment of degreasing and wire-brushing, the 1-mm-thick 90 pct cold-rolled samples were stacked to be 2 mm thick and roll-bonded by 50 pct reduction in one pass. The roll-bonded sheet was cut to be half in length, and subject to the next roll-bonding process. A procedure of cutting, surface treatment, stacking, and roll-bonding is referred to as 1 cycle of ARB, and the ARB process was repeated up to 7 cycles. Since an equivalent strain of 0.8 is introduced in each cycle of ARB, the total equivalent strain achieved by 90 pct cold rolling followed by 7-cycles of ARB is 8.3. For both cold rolling and ARB, rolled samples were water-cooled immediately after each rolling pass and stored in a freezer at − 50 °C unless the samples were subject to experiments, to minimize any structural changes such as recovery or boundary migration during the storage.

In this paper, hereafter, the 50 and 90 pct cold-rolled samples are termed as CR50 and CR90 samples, respectively, and the samples 90 pct cold-rolled and ARB processed by 3, 5, and 7 cycles are termed as CR90 + 3c ARB, CR90 + 5c ARB, and CR90 + 7c ARB samples, respectively.

C. *Annealing*

Samples deformed to different strains were annealed to reduce the dislocation density as well as to change the grain/sub-grain size. For all samples, multi-step annealing[42] was applied. The multi-step annealing is a combination of several steps of low-temperature, long-time annealing, and high-temperature annealing. The annealing conditions varied depending on the amount of strain applied before annealing. The objective of multi-step annealing is to reduce dislocation density by relatively low-temperature annealing, and to lead to gradual structural coarsening without discontinuous recrystallization by subsequent high-temperature annealing.

Figure 1 shows annealing conditions for samples deformed to different strains. CR50 samples were annealed at 175 °C for 24 hours, followed by annealing for 0.5 hours at different temperatures in the range of 200 to 275 °C. For CR90 and CR90 + 3c ARB samples, annealing was carried out at 75 °C, 100 °C, 125 °C, 150 °C, and 175 °C in multi-steps where the annealing time was set for 24 hours in each step. For CR90 + 5c ARB samples, annealing was carried out at 125 °C, 150 °C, and 175°C for 24 hours in multi-steps, followed by high-temperature annealing for 0.5 hours in the range of 200 to 600 °C.

D. *Electron Backscatter Diffraction (EBSD)*

Microstructures of the deformed and annealed samples were characterized by EBSD. Cross sections perpendicular to the transverse direction (TD) of the rolled samples were mechanically polished by SiC emery papers and then electrically polished at a voltage of 20 V and at – 15 °C in a solution of 100 mL $HClO_4$ + 900 mL C_2H_5OH, and subjected to the EBSD measurements. EBSD measurements were carried out in a JEOL JSM-7001F SEM with a field emission gun operating at
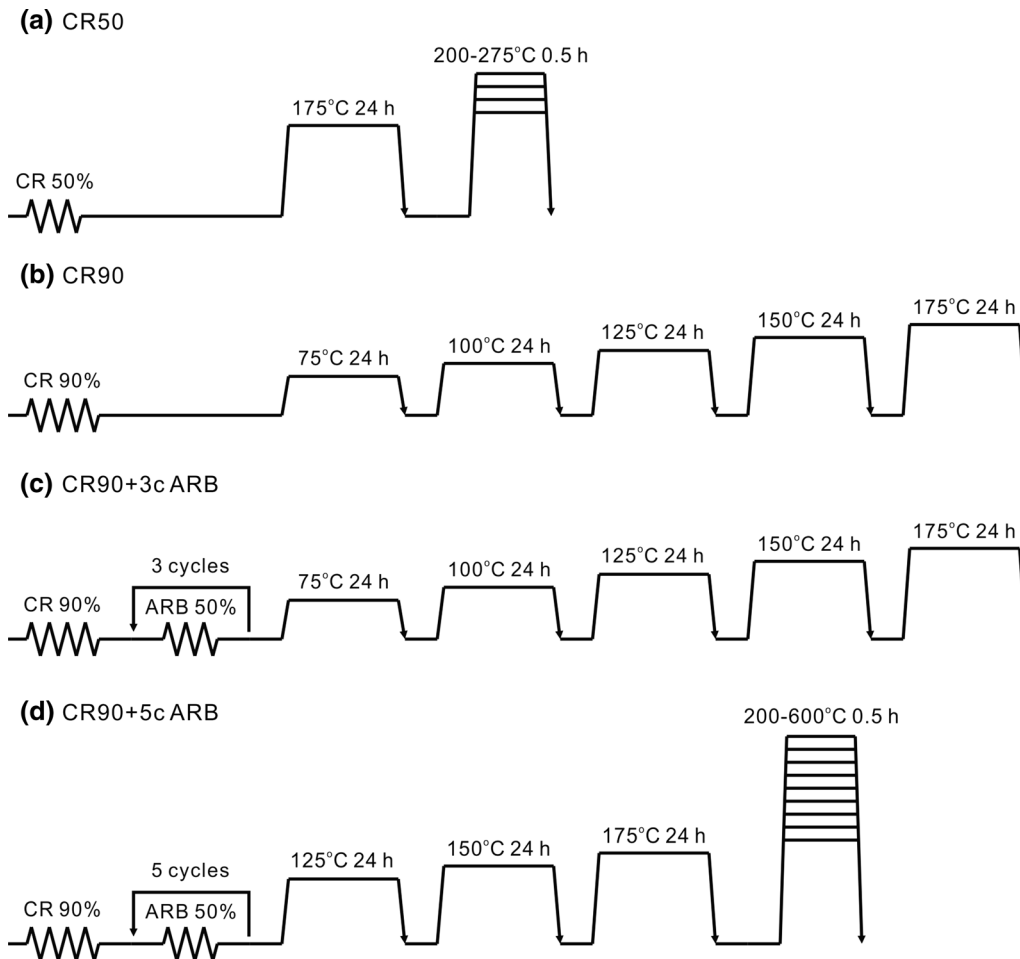
Fig. 1—Annealing conditions for (*a*) CR50, (*b*) CR90, (*c*) CR90 + 3c ARB, and (*d*) CR90 + 5c ARB samples.

15 kV using a program TSL OIM Data Collection ver. 6, where the step size varied in the range of 0.05 to 1 μm depending on the size of structure and scanned area. The EBSD data obtained were analyzed using a program TSL OIM Analysis ver. 6. For the analysis, boundaries below 2 deg were ignored to remove the inaccuracy for misorientation angle determination of such low-angle boundaries.

E. Transmission Electron Microscopy (TEM)

For TEM observations, thin foils perpendicular to the TD were prepared by mechanical polishing followed by electro-polishing in the same way as the EBSD sample preparation. An FEI CM300 TEM operating at 300 kV was used for structural observation.

F. Determination of Structural Parameters

Using the obtained EBSD and TEM results, microstructural parameters were determined in the following way.

1. Dislocation density

For as-deformed samples, individual dislocations between the boundaries were observed under multi-beam diffraction conditions in TEM to reveal all dislocations within a grain. The density of dislocations within individual grains was determined by the linear intercept method from the TEM images.[43] The foil thickness required for the dislocation density determination was estimated by convergent beam electron diffraction. At least 10 grains were subjected to dislocation density measurements, and the average dislocation density was obtained for each deformation condition.

2. Determination of boundary spacing

In general, the term ''grain size'' is used to describe the structural size for recrystallized structures. However, in this work, not only recrystallized structures but deformed and recovered structures are also considered. Thus, instead of ''grain size,'' we use the term ''boundary spacing'' to describe all structural sizes, including grain size for recrystallized structures, sub-grain size for recovered structures, and dislocation cell size for as-deformed structures.

Boundary spacing was measured by the linear intercept method. Two sets of parallel test lines along the ND and RD were drawn on the EBSD boundary maps or TEM images. Boundary spacings along the ND and RD are called boundary thickness (d_t) and boundary length (d_l), respectively. Boundary spacing along random test lines (d_R) was determined in the following way. The number of intercepts per unit length along random test lines ($N_{L,R}$) can be estimated as an average of the number of intercepts per unit length on test lines along ND ($N_{L,ND}$) and RD ($N_{L,RD}$), as follows:

$$N_{L,R} = \frac{N_{L,ND} + N_{L,RD}}{2}. \qquad [2]$$

Note that $N_{L,ND}$, $N_{L,RD}$ and $N_{L,R}$ can be written as $1/d_t$, $1/d_l$, and $1/d_R$, respectively. Therefore, d_R can be written as,

$$d_R = \frac{2}{\frac{1}{d_t} + \frac{1}{d_l}}. \qquad [3]$$

3. Determination of boundary fraction

In this paper, the following procedure has been applied to estimate boundary fraction in different angle ranges.

Fraction of boundaries with misorientation angles above a critical angle θ_c can be given by,

$$f_{\theta > \theta_c} = \frac{N_{L,\theta > \theta_c}}{N_{L,ALL}}, \qquad [4]$$

where $N_{L,ALL}$ is the number of all boundaries per unit length on test lines, and $N_{L,\theta > \theta_c}$ is the number of boundaries with misorientation angles above θ_c per unit length, respectively. Note that $N_{L,ALL}$ and $N_{L,\theta > \theta_c}$ can be written as,

$$d_{ALL} = \frac{1}{N_{L,ALL}}, \quad d_{\theta > \theta_c} = \frac{1}{N_{L,\theta > \theta_c}}, \qquad [5]$$

where d_{ALL} is the average spacing of all boundaries, and $d_{\theta > \theta_c}$ is the average spacing of boundaries with misorientation angles above θ_c. From Eqs. [4] and [5], the fraction of boundaries with misorientation angles above θ_c can be estimated as,

$$f_{\theta > \theta_c} = \frac{d_{ALL}}{d_{\theta > \theta_c}}. \qquad [6]$$

In this paper, d_{ALL} is replaced by the spacing of all boundaries along ND determined by TEM, $d_{t,ALL}$, and $d_{\theta > \theta_c}$ is replaced by the spacing of boundaries above θ_c along ND determined by EBSD, $d_{t,\theta > \theta_c}$. The critical angles θ_c of 0 deg, 2 deg, 5 deg, 10 deg, and 15 deg were used in the analysis of this study. Figure 2 is a schematic illustration showing how to determine the spacing of boundaries with misorientation angles above θ_c. From the TEM images, $d_{t,ALL}$ was determined and from the EBSD boundary maps, $d_{\theta > \theta_c}$ was determined, where the critical angle varied from 2 deg to 15 deg.

G. Tensile Test

Mechanical properties were determined by uniaxial tensile tests using a Shimadzu AG-5000B. From the deformed and annealed samples, tensile test specimens with a gauge 10 mm in length, 5 mm in width, and 1 mm in thickness were prepared, where the tensile axis is parallel to the RD of the samples. The tensile tests were carried out at room temperature at a constant crosshead speed of 0.5 mm min^{-1}, corresponding to an initial strain rate of 8.3×10^{-4} s^{-1}. Tensile elongation was measured by a strain gauge-type clip-on extensometer Shimadzu SG10-100.

III. RESULTS

A. Microstructures

1. As-deformed state

Microstructures of the as-deformed samples were characterized by TEM observations and EBSD measurements. Typical TEM images are shown in Figures 3(a), (e), (i), (m), and the boundary maps obtained from the EBSD are shown in Figure 4. Quantified structural parameters (boundary spacing, fraction of boundaries, and dislocation density) from these results are summarized in Table I and plotted as a function of strain in Figure 5. In Figure 5(c), standard deviation of dislocation density was shown as error bars.

Figures 3(a), (e), (i), (m) show TEM images of samples deformed to different strains. In the figure, boundary spacing along random test lines ($d_{R,ALL}$) is indicated. The CR50 sample (Figure 3(a)) shows a dislocation cell structure with a high density of dislocations between the cell boundaries, where the cell size is as small as 0.84 μm. The boundary spacing gradually decreases with increasing the strain and reaches a minimum of ~ 0.5 μm in the CR90 and CR90 + 3c ARB samples (Figures 3(e), (i), 5(a)). When 90 pct rolling is followed by 5-cycle ARB (Figure 3(m)), a relatively equiaxed ultrafine structure is observed. It is also seen that dislocation density between the boundaries is relatively low, and that the boundaries are very sharp, compared with low-strained samples. Such a structure is quite similar to that obtained by 99.99 pct aluminum deformed by other SPD processes.[42,44–46] It should be noted that the average boundary spacing in the CR90 + 5c ARB sample is slightly larger than in the CR90 + 3c ARB sample (Table I; Figure 5(a)), indicating that boundary migration took place during rolling deformation in the high strain.

Dislocation density between the boundaries (ρ_0) was determined from the TEM and is summarized in Table I and Figure 5(c). The dislocation density increases with increasing the strain up to 90 pct cold rolling, but it tends to decrease by further deformation, resulting in a relatively clean ultrafine structure in the CR90 + 5c ARB sample (see Figure 3(m)). This indicates that dislocation annihilation process was enhanced in the high strain.

Figure 4 shows grain boundary maps obtained from the EBSD measurements. In the maps, high-angle boundaries with misorientation angles above 15 deg
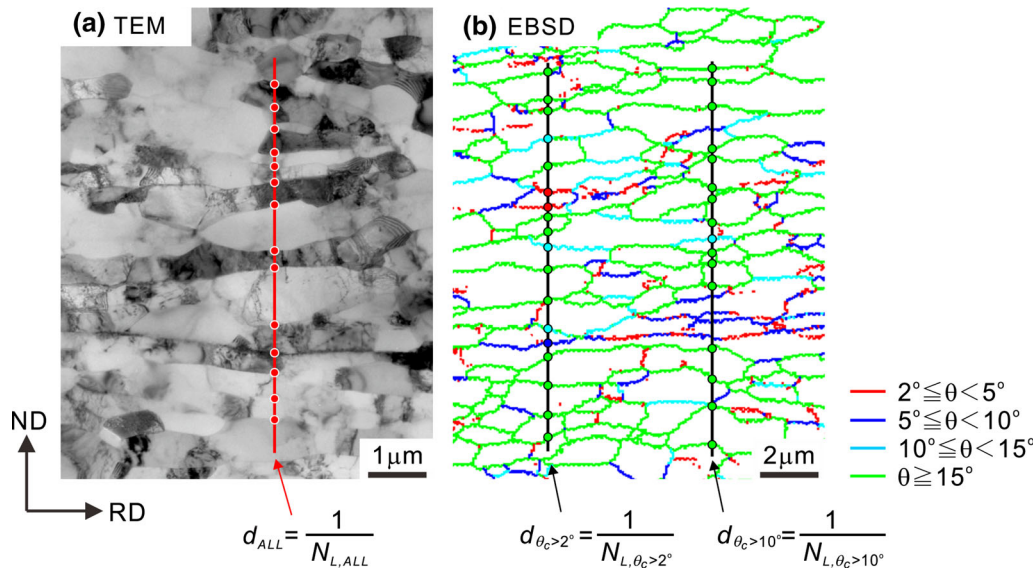
Fig. 2—Determination of average spacing of boundaries with misorientation angles above a critical angle θ_c. (a) TEM image and (b) EBSD map for as-deformed CR90 + 7c ARB sample, as an example.

are indicated by green lines, while low-angle boundaries with misorientation angles below 15 deg are indicated by red lines. The CR50 and CR90 samples (Figures 4(a) and (b)) are dominated by low-angle boundaries, although small number of pre-existing high-angle boundaries in the undeformed initial structure can be observed. By further deformation, the structure is gradually being divided by deformation-induced high-angle boundaries (Figure 4(c)), and finally an elongated structure dominated by high-angle boundaries is observed in the CR90 + 5c ARB sample (Figure 4(d)).

The spacing of boundaries with misorientation angles above 15 deg along ND is plotted as a function of strain in Figure 5(a). As was observed from the images in Figure 4, the spacing of boundaries above 15 deg decreases with increasing the strain, but when 90 pct cold rolling is followed by 5-cycles of ARB, which corresponds to an equivalent strain of 6.7, the spacing becomes saturated at approximately 1 μm.

Fraction of boundaries with misorientation angles above a critical angle θ_c was calculated by $d_{t,ALL}/d_{\theta > \theta_c}$ and summarized in Table I. The fraction of high-angle boundaries (> 15 deg) is only shown in Figure 5(b). If we focus on the change in the fraction of boundaries with misorientation angles above 15 deg, the fraction of boundaries (> 15 deg) gradually increases with increasing the applied strain, as can also be observed in Figure 4, but the fraction becomes saturated at approximately 50 pct when 90 pct cold rolling is followed by 5 cycles of ARB.

The above microstructural observations for the as-deformed samples demonstrate that an equivalent strain of 6.7 should be introduced to produce ultrafine-grained structure dominated by high-angle boundaries with misorientation angles above 15 deg, but further deformation by a strain of above 6.7 leads to a structural saturation due to a balance of dislocation multiplication and annihilation as well as a balance of introduction of deformation-induced high-angle boundaries and migration of high-angle boundaries during deformation.

2. *Annealed state*
In order to produce sub-grained structure dominated by low-angle boundaries and ultrafine-grained structure dominated by high-angle boundaries, annealing treatments have been carried out for the CR50, CR90, CR90 + 3c ARB, and CR90 + 5c ARB samples. The reason why these four series of deformed samples were chosen for annealing is a variety of fraction of high-angle boundaries in the as-deformed states.

When the CR50 sample is annealed at 175 °C for 24 hours (Figure 3(b)), dislocation annihilation mainly takes place between the dislocation cell boundaries and in the cell boundaries, leading to a typical sub-grained structure subdivided by sharp dislocation boundaries with few individual dislocations between the boundaries. A slight sub-grain coarsening occurs by further annealing at higher temperatures (Figures 3(c) and (d)). Microstructural changes during annealing of CR90 and CR90 + 3c ARB samples (Figure 3(e) through (l)) are qualitatively similar to those of CR50 sample. Namely, recovery of dislocations is a dominant process in the early stage of annealing, leading to sub-grained structures with few dislocations between the sub-grain boundaries, while slight sub-grain coarsening occurs by higher-temperature annealing. On the other hand, in the case of CR90 + 5c ARB sample, gradual structural coarsening, in addition to dislocation annihilation, occurs during annealing from low to high temperatures (Figures 3(m) through (p)).

To realize further structural coarsening, annealing at much higher temperatures was carried out. However, for CR50, CR90, and CR90 + 3c ARB samples, discontinuous recrystallization took place, resulting in unwanted
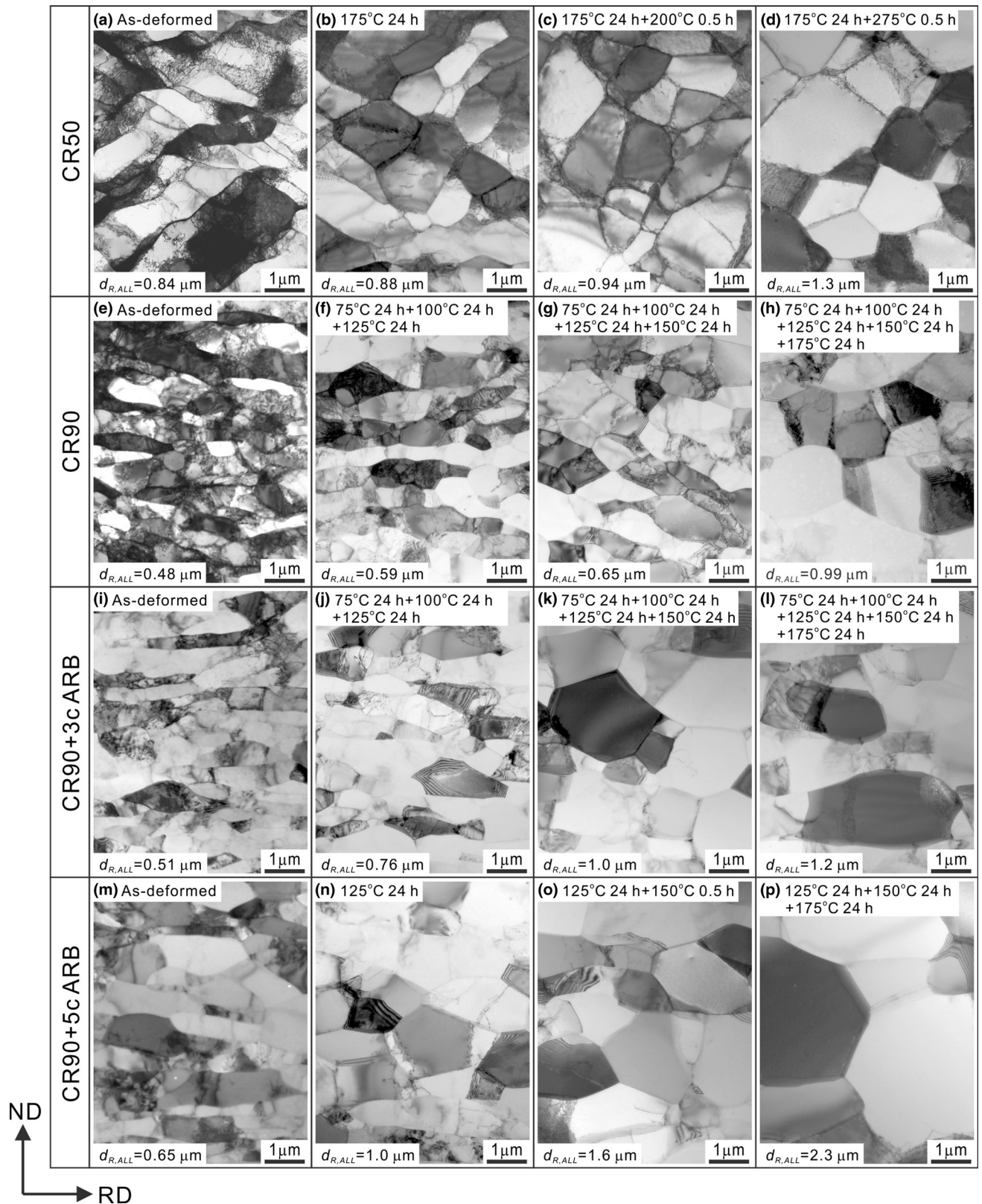
Fig. 3—TEM images of deformed and annealed samples. (*a* through *d*) CR50, (*e* through *h*) CR90, (*i* through *l*) CR90 + 3c ARB, and (*m* through *p*) CR90 + 5c ARB samples.
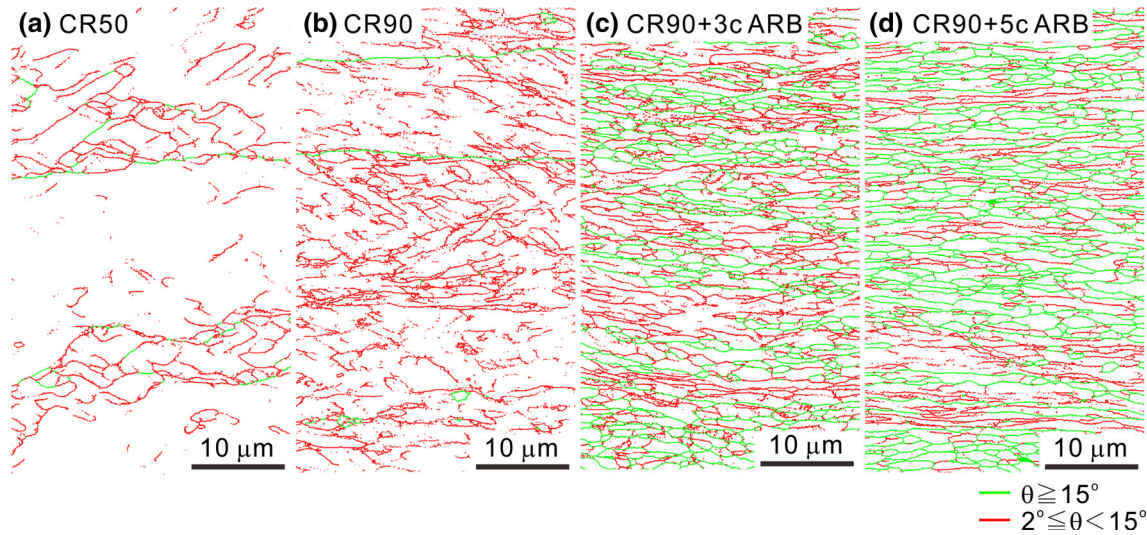
Fig. 4—Grain boundary maps obtained from EBSD measurements for samples deformed to different strains. (*a*) CR50, (*b*) CR90, (*c*) CR90 + 3c ARB, and (*d*) CR90 + 5c ARB (Color figure online).

Table I.   Structural Parameters for As-deformed Samples

Sample Names	ε_{eq}	$d_{t,ALL}$ (μm)	$d_{l,ALL}$ (μm)	$d_{R,ALL}$ (μm)	$f_{\theta > 2\ deg}$ (Pct)	$f_{\theta > 5\ deg}$ (Pct)	$f_{\theta > 10\ deg}$ (Pct)	$f_{\theta > 15\ deg}$ (Pct)	ρ_0 (m^{-2})
Undeformed	0	138	195	162	100	95.3	83.3	79.3	not measured
CR50	0.8	0.70	1.0	0.84	28.6	16.6	1.4	0.9	9.7×10^{12}
CR90	2.7	0.36	0.72	0.48	35.6	9.5	5.1	4.5	4.4×10^{13}
CR90 + 3c ARB	5.1	0.35	0.91	0.51	59.3	44.1	33.4	28.8	2.1×10^{13}
CR90 + 5c ARB	6.7	0.49	0.95	0.65	85.8	72.3	58.5	49.3	2.7×10^{13}
CR90 + 7c ARB	8.3	0.51	0.97	0.67	81.7	71.4	58.5	50.6	1.7×10^{13}

ε_{eq}: total equivalent strain, $d_{t,ALL}$ and $d_{l,ALL}$: boundary spacing along the ND and RD, respectively, $d_{R,ALL}$: boundary spacing by random intercept method, $f_{\theta > 2\ deg}$: fraction of boundaries (> 2 deg) estimated by $d_{t,ALL}/d_{t,\theta > 2\ deg}$, $f_{\theta > 5\ deg}$: fraction of boundaries (> 5 deg) estimated by $d_{t,ALL}/d_{t,\theta > 5\ deg}$, $f_{\theta > 10\ deg}$: fraction of boundaries (> 10 deg) estimated by $d_{t,ALL}/d_{t,\theta > 10\ deg}$, $f_{\theta > 15\ deg}$: fraction of boundaries (> 15 deg) estimated by $d_{t,ALL}/d_{t,\theta > 15\ deg}$, ρ_0: dislocation density between the boundaries.

heterogeneous microstructures. On the contrary, in the CR90 + 5c ARB sample, higher-temperature annealing successfully led to relatively uniform structural coarsening without discontinuous recrystallization. As a result, homogeneous structures with relatively uniform grain size distribution were successfully obtained in the average grain size range of 0.65 to 69 μm. Such uniform structural coarsening by multi-step annealing for the CR90 + 5c ARB sample is in good agreement with that for 6-cycle ARB aluminum samples reported in the previous work.[10,42]

B. Stress–Strain Curves

1. As-deformed state

For the as-deformed samples, tensile test at room temperature was carried out and the obtained nominal stress–strain curves are shown in Figure 6. 0.2 Pct proof stress was defined as yield stress for the as-deformed samples. The yield stress and ultimate tensile strength of undeformed starting sample are 19.0 and 41.6 MPa, respectively. The strength significantly increases by 50 pct cold rolling and gradually increases with increasing the strain, and it shows a maximum after 90 pct cold

rolling. The yield stress and ultimate tensile strength of CR90 samples are 120 and 134 MPa, respectively. However, the strength slightly decreases by further deformation. Such deformation-induced softening in high strain deformation has also been observed in aluminum samples with purities of 99.99 pct and higher processed by severe plastic deformation, such as high pressure torsion,[45,47] equal channel angular extrusion,[48] ARB,[44] accumulative channel-die compression bonding.[46] As was shown in Figure 3 and Table I, the increase in boundary spacing and the decrease in dislocation density were observed in high strain deformation, which should be responsible for the deformation-induced softening, which will be discussed in detail later in Section IV–A.

In terms of ductility, uniform elongation significantly decreases from 27.4 pct in the undeformed sample to 0.75 pct by 50 pct cold rolling, and it does not change so much by further deformation to high strain. Total elongation also suddenly decreases from 41.0 to 9.6 pct by 50 pct cold rolling, but it tends to increase gradually with increasing the strain by further deformation. Since there is no significant change in the uniform elongation by an increase in the applied strain, this change in total
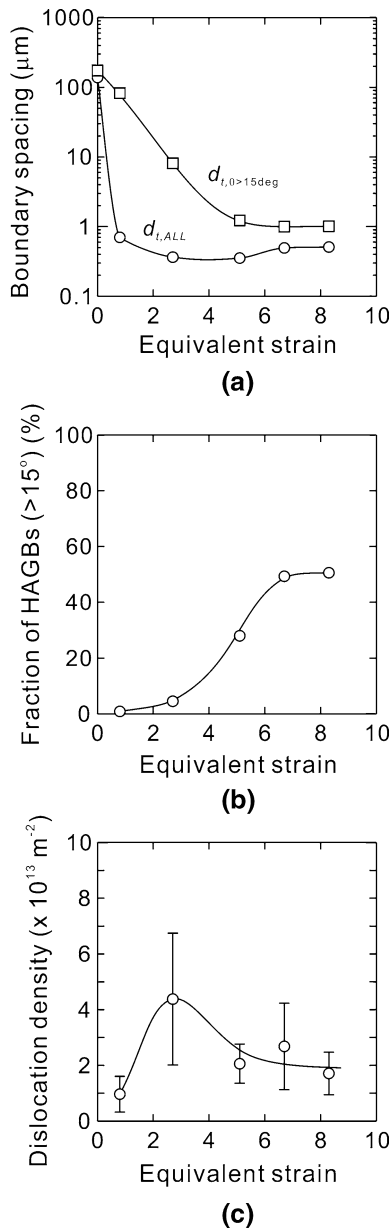
(a)

(b)

(c)

Fig. 5—(*a*) Boundary spacing, (*b*) fraction of high-angle boundaries (> 15 deg), and (*c*) dislocation density between the boundaries for as-deformed samples.
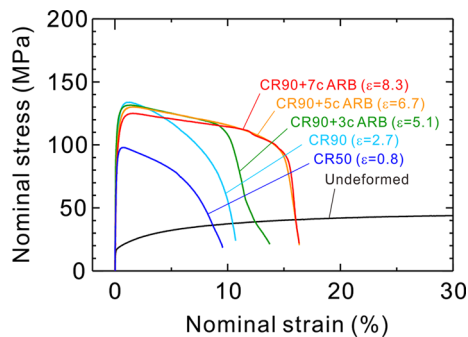

Fig. 6—Nominal stress–strain curves for as-deformed samples.

elongation is mainly due to the change in post-uniform elongation. A similar tendency of significant improvement of post-uniform elongation by high strain deformation has been reported in high-purity aluminum and copper samples in previous works.[49–51] Two possible mechanisms have been proposed to understand this phenomenon: grain boundary sliding[49] and enhanced dynamic recovery at narrowly spaced high-angle grain boundaries[50,51] during tensile test. At the moment, experimental evidences are not sufficient to reach any decisive conclusions, and further investigations are necessary to understand this issue.

2. Annealed state

For the annealed samples, tensile tests were carried out at room temperature, where the tests were done only for annealed samples with relatively uniform structural distributions. The obtained nominal stress–strain curves are shown in Figure 7. From the nominal stress–strain curves, yield stress (σ_y), ultimate tensile strength (σ_{UTS}), uniform elongation ($e_{uniform}$), and total elongation (e_{total}) were determined and summarized in Table II, where detailed annealing conditions and corresponding boundary spacing are also demonstrated. To avoid the complexity, the boundary spacing is only indicated in Figure 7. From the stress–strain curves, yielding behavior has been classified into continuous and discontinuous yielding. As the definition of yield stress, 0.2 pct proof stress is used for continuous yielding and lower yield point is used for discontinuous yielding.

In the CR50 samples (Figure 7(a)), the strength of as-deformed sample significantly decreases by annealing at 175 °C for 24 hours. This could mainly be due to a significant decrease in dislocation density (see Figure 3(b)). Further annealing at higher temperatures leads to a gradual decrease in strength, which could be due to a slight sub-grain coarsening (see Figures 3(c) and (d)). It is also seen that the elongation gradually increases with increasing the boundary spacing.

The change in strength and ductility during annealing in the CR90 samples (Figure 7(b)) is qualitatively similar to that in the CR50 samples. A significant decrease in strength by low-temperature, long-time annealing of 75 °C to 125 °C 24 h would mainly be caused by recovery of dislocations (see Figure 3(f)), and further annealing leads to gradual decrease in strength, which would be related to sub-grain coarsening (see Figures 3(g) and (h)). The elongation tends to increase with increasing the boundary spacing, as for the CR50 samples.

In the CR90 + 3c ARB samples (Figure 7(c)), the strength gradually decreases during annealing, due to dislocation annihilation followed by sub-grain coarsening (see Figures 3(i) through (l)). This tendency is basically similar to that in the CR50 and CR90 samples. On the other hand, the elongation decreases during annealing, in contrast to the behavior of CR50 and CR90 samples. Another interesting result observed in Figure 7(c) is that discontinuous yielding took place in the sample with the average boundary spacing of 1.2 μm.

In the CR90 + 5c ARB samples (Figure 7(d)), the strength decreases significantly by annealing of 125 °C
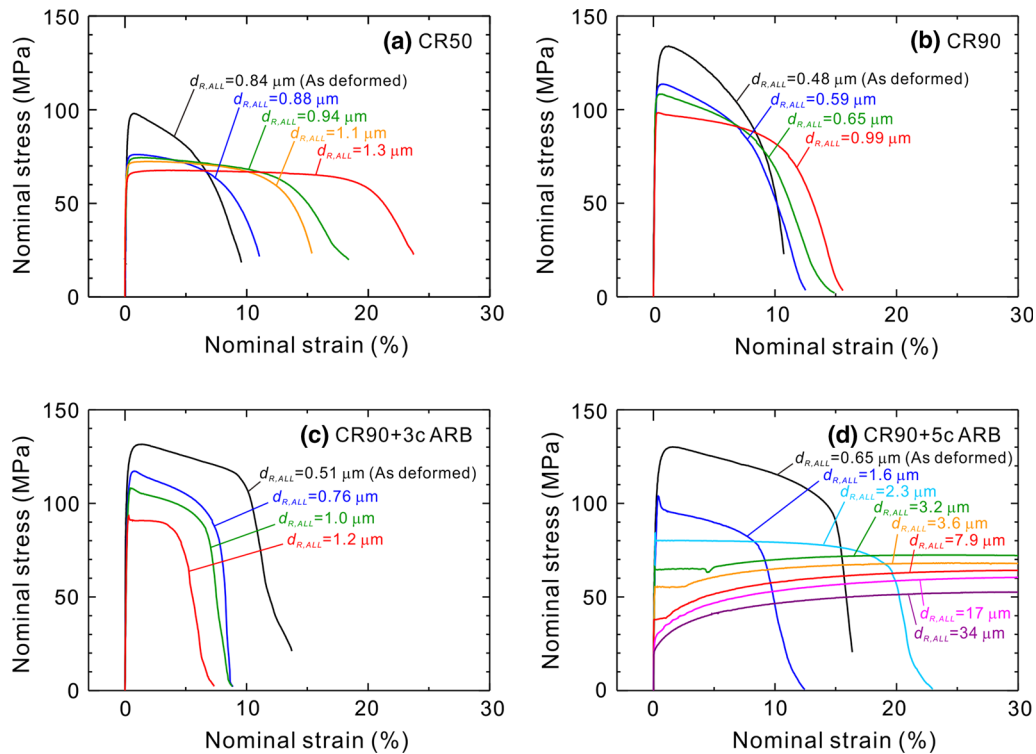
Fig. 7—Nominal stress–strain curves for deformed and annealed samples. (*a*) CR50, (*b*) CR90, (*c*) CR90 + 3c ARB, and (*d*) CR90 + 5c ARB samples Adopted from Ref. [33].

24 h + 150 °C 24 h, which is due to recovery and structural coarsening (see Figure 3(o)). Subsequent annealing at higher temperatures leads to gradual structural coarsening, so that the strength also gradually decreases with increasing the average boundary spacing. It should be noted here that distinct discontinuous yielding is observed when the average boundary spacing is in the range from 1.6 to 7.9 μm. However, if the boundary spacing is above approximately 10 μm, conventional continuous yielding behavior is observed. In terms of the change in ductility, elongation decreases during annealing from the as-deformed sample to the sample annealed at 125 °C 24 h + 150 °C 24 h, in good agreement with the case for CR90 + 3c ARB samples in Figure 7(c). When the boundary spacing is larger than 2 μm, elongation starts to increase with increasing the boundary spacing. These tendencies in tensile behavior in the CR90 + 5c ARB and annealed samples are good agreement with those in the 6-cycle ARB and annealed samples.[10]

C. Hall–Petch Relationship

To understand the effect of boundary misorientation as well as boundary spacing on yield stress, the Hall–Petch relationship is investigated for the obtained samples. The yield stress is plotted as a function of reciprocal square root of average boundary spacing in Figure 8. In this figure, the data of high-purity aluminum in the previous work[10] are also plotted, where the samples were produced by 6-cycles of ARB without

lubrication followed by annealing. In addition, in order to increase the reliability, samples with different grain sizes were re-produced again in this study by using the similar experimental procedure in Reference 10, and the data are plotted in the figure. For comparison, the data of fully recrystallized structures with different average grain sizes in the range of 40 to 405 μm[10] are also plotted in the figure, where these fully recrystallized samples were produced by 50 pct cold rolling followed by annealing for 0.5 hours at different temperatures in the range of 325 °C to 625 °C. Note that in Figure 8, the samples are classified into three categories, depending on the fraction of high-angle boundaries with misorientation angles above 15 deg. The samples with a fraction of high-angle boundaries below 30 pct, between 30 and 60 pct and above 60 pct are plotted as red, blue, and green marks, respectively. It should also be noted that the data of the well-annealed samples with few dislocations between the boundaries are plotted as solid marks, and the data of the as-deformed samples are plotted as dotted marks.

It is seen that data points for coarse-grained samples with an average grain around 20 μm and above can be explained by a single Hall–Petch curve, independent of the fraction of high-angle boundaries. The dashed line is an approximated Hall–Petch curve for the coarse-grained samples, where the slope of the curve is 41 MPa μm$^{1/2}$.[10] This suggests that in coarse-grained region, the yield stress can be determined only by the grain size, regardless of the misorientation angles of the boundaries.

However, in the grain size range less than 20 μm, the strength of all samples is positively deviated from the extrapolation of the Hall–Petch curve in the coarse grains. Moreover, it should be emphasized that the strength of well-annealed ultrafine-grained samples, with the fraction of high-angle boundaries of more than 30 pct, becomes significantly higher, leading to a larger Hall–Petch slope than that of coarse grains. The dotted line is an approximated Hall–Petch curve for the ultrafine-grained samples, where the slope is 131 MPa μm$^{1/2}$, about three times larger than that of coarse grains. This behavior can be termed as extra Hall–Petch strengthening, as was described in the Introduction. By comparing these plots with the yielding behavior in stress–strain curve, it can be confirmed that the samples with such a large Hall–Petch slope correspond to those who reveal a clear discontinuous yielding. Thus, the extra Hall–Petch strengthening observed in the well-annealed ultrafine-grained samples should be due to the occurrence of the unexpected discontinuous yielding, in good agreement with the previous works.[9–14]

On the other hand, the sub-grained samples with the fraction of high-angle boundaries less than 30 pct and the as-deformed samples also reveal extra Hall–Petch strengthening, but these samples are much weaker than the well-annealed ultrafine-grained samples. It is also seen that the Hall–Petch strengthening is larger with increasing the applied strain, *i.e.*, with increasing the fraction of high-angle boundaries. These results indicate that high-angle boundaries are more effective for strengthening than low-angle sub-grain boundaries in the fine grain size range.

IV. DISCUSSION

In this work, high-purity aluminum samples with different grain/sub-grain size, boundary misorientation, and dislocation density were produced, and the mechanical properties were systematically investigated. The interesting behaviors observed can be summarized as follows:

- The strength of as-deformed samples increased with increasing the applied strain in the low strain, but deformation-induced softening was observed in the high strain (Figure 6).
- Ultrafine-grained samples dominated by high-angle boundaries, with the average grain size of 1 to 10 μm, showed unusual discontinuous yielding, while sub-grained samples dominated by low-angle dislocation boundaries revealed continuous yielding (Figure 7).
- The extra Hall–Petch strengthening was observed in both ultrafine-grained samples dominated by high-angle boundaries and sub-grained samples dominated by low-angle boundaries, but the yield stress of the sub-grained samples was lower than that of the ultrafine-grained samples at the same structural size (Figure 8).

The mechanisms of these behaviors are discussed in detail in the following.

A. *Origin of Deformation-Induced Softening*

In this section, we discuss the strengthening mechanisms of the as-deformed samples in order to understand the origin of deformation-induced softening in the high strain deformation observed in Figure 6. For this purpose, we try to calculate the yield stress of the samples based on the characteristics of deformation microstructures.

For the calculation of yield stress, it is assumed that strengthening contributions from dislocations and grain boundaries can simply be additive, where precipitation strengthening is ignored due to the high purity of the material. Thus, the yield stress of materials can be written as,

$$\sigma_y = \sigma_0 + \sigma_{dis} + \sigma_{gb}, \qquad [7]$$

where σ_0 is the friction stress, σ_{dis} is the contribution from dislocations, and σ_{gb} is the contribution from grain boundaries. Note that solid solution strengthening from small amount of impurities is included in the friction stress σ_0.

Based on the Bailey–Hirsch relationship for dislocation strengthening[52] and Hall–Petch relationship for grain boundary strengthening,[1,2] Eq. [7] can be rewritten as,

$$\sigma_y = \sigma_0 + M\alpha Gb\sqrt{\rho_0 + \rho_{dis}} + k d_{gb}^{-1/2}, \qquad [8]$$

where M is the Taylor factor, α is a constant, G is the shear modulus, b is the Burges vector, ρ_0 is the density of individual dislocations between the boundaries, ρ_{dis} is the density of dislocations stored in low-angle dislocation boundaries, k is the Hall–Petch coefficient, and d_{gb} is the average spacing of boundaries that contribute as grain boundary strengthening.

In this calculation, we consider a critical angle θ_c to separate dislocation strengthening from grain boundary strengthening. We assume that when misorientation angles of boundaries are smaller than θ_c such boundaries contribute as dislocation strengthening based on the Bailey–Hirsch relationship, while boundaries with misorientation angles larger than θ_c are assumed to act as conventional grain boundaries that contribute as the Hall–Petch strengthening. Based on this assumption, Eq. [8] can be transformed as,[10,53]

$$\sigma_y = \sigma_0 + M\alpha Gb\sqrt{\rho_0 + \frac{3(1 - f_{\theta > \theta_c})\theta_{ave,\theta < \theta_c}}{b d_{R,ALL}}}$$
$$+ k\sqrt{\frac{f_{\theta > \theta_c}}{d_{R,ALL}}}, \qquad [9]$$

where $f_{\theta > \theta_c}$ is the fraction of boundaries with misorientation angles above θ_c, $\theta_{ave,\theta < \theta_c}$ is the average misorientation angle of the boundaries with misorientation angles below θ_c, $d_{R,ALL}$ is the random boundary spacing determined by TEM. For calculation using Eq. [9], the

Table II. Mechanical Properties for Deformed and Annealed Samples

| Deformation Conditions	Annealing Conditions	$d_{R,ALL}$ (μm)	Yielding Behavior	σ_y (MPa)	σ_{UTS} (MPa)	$e_{uniform}$ (Pct)	e_{total} (Pct)
CR50	as deformed	0.84	continuous	94.0	98.0	0.75	9.6
	175 °C 24 h	0.88	continuous	74.6	76.2	1.0	11.0
	175 °C 24 h + 200 °C 0.5 h	0.94	continuous	76.5	74.5	1.3	18.4
	175 °C 24 h + 250 °C 0.5 h	1.1	continuous	70.9	72.3	2.2	15.3
	175 °C 24 h + 275 °C 0.5 h	1.3	continuous	64.1	67.7	4.0	23.7
CR90	as deformed	0.48	continuous	120	134	1.3	10.7
	75 °C 24 h + 100 °C 24 h + 125 °C 24 h	0.59	continuous	112	114	0.81	12.3
	75 °C 24 h + 100 °C 24 h + 125 °C 24 h + 150 °C 24 h	0.65	continuous	108	108	0.64	14.9
	75 °C 24 h + 100 °C 24 h + 125 °C 24 h + 150 °C 24 h + 175 °C 24 h	0.99	continuous	98.0	98.0	0.43	15.6
CR90 + 3c ARB	as deformed	0.51	continuous	118	132	1.4	13.7
	75 °C 24 h + 100 °C 24 h + 125 °C 24 h	0.76	continuous	111	117	0.80	9.1
	75 °C 24 h + 100 °C 24 h + 125 °C 24 h + 150 °C 24 h	1.0	continuous	105	108	0.46	9.1
	75 °C 24 h + 100 °C 24 h + 125 °C 24 h + 150 °C 24 h + 175 °C 24 h	1.2	discontinuous	91.2	93.4	0.29	7.5
CR90 + 5c ARB	as deformed	0.65	continuous	108	130	1.6	16.4
	125 °C 24 h + 150 °C 24 h	1.6	discontinuous	97.3	103	0.41	9.7
	125 °C 24 h + 150 °C 24 h + 175 °C 24 h	2.3	discontinuous	81.2	84.8	0.17	27.9
	125 °C 24 h + 150 °C 24 h + 175 °C 24 h + 200 °C 0.5 h	3.2	discontinuous	64.8	73.1	23.6	48.4
	125 °C 24 h + 150 °C 24 h + 175 °C 24 h + 250 °C 0.5 h	3.6	discontinuous	55.3	68.3	25.9	51.4
	125 °C 24 h + 150 °C 24 h + 175 °C 24 h + 275 °C 0.5 h	7.9	discontinuous	36.3	63.3	31.7	45.6
	125 °C 24 h + 150 °C 24 h + 175 °C 24 h + 300 °C 0.5 h	17	continuous	26.7	59.1	35.2	56.4
	125 °C 24 h + 150 °C 24 h + 175 °C 24 h + 400 °C 0.5 h	34	continuous	22.8	54.2	33.9	55.1
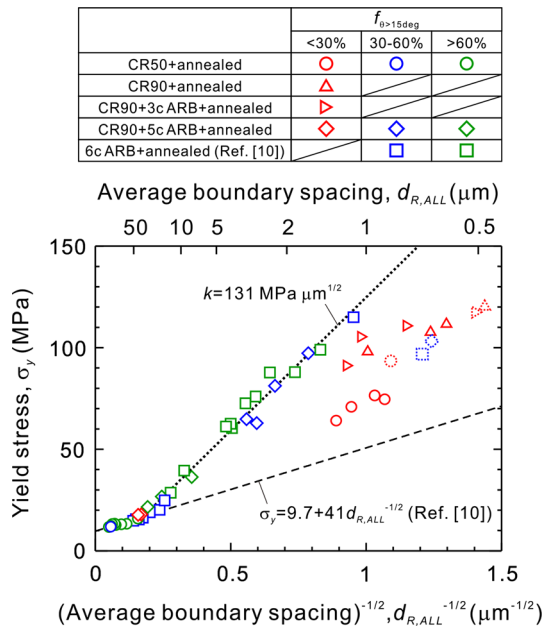
Fig. 8—Hall–Petch relation in samples deformed to different strains and annealed. Dotted marks are for the as-deformed samples Adopted from Ref. [33] (Color figure online).
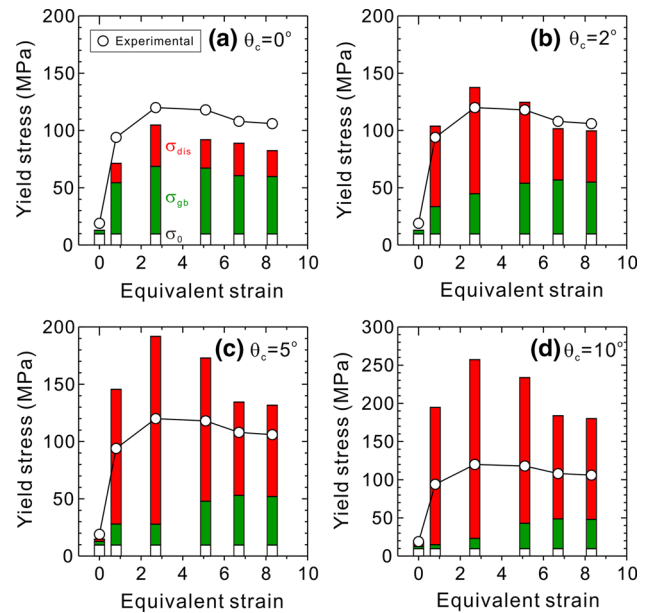

Fig. 9—Structure-based yield stress calculation for samples deformed to different strains, assuming that strengthening contributions from dislocations and grain boundaries are simply additive. The critical angle to separate between dislocation boundaries and grain boundaries (θ_c) varies from (a) 0 deg, (b) 2 deg, (c) 5 deg, and (d) 10 deg (Color figure online).

following parameters were used. For pure Al, α of 0.24,[54] G of 26 GPa,[55] b of 0.286 nm were used. As the Taylor factor, M of 3.06[56] was used, which is the average value of random-textured fcc metals. From the Hall–Petch relationship in coarse-grained pure Al,[10] σ_0 of 9.7 MPa and k of 41 MPa $\mu m^{1/2}$ were used. For strength calculation, we set a critical angle as 0 deg, 2 deg, 5 deg, 10 deg, and 15 deg to separate low-angle boundaries that contribute as dislocation strengthening from boundaries that contribute as conventional grain boundary strengthening.

For the strength calculation in the as-deformed samples, the parameters in Table I were used for ρ_0 and $d_{R,ALL}$ and $f_{\theta > \theta_c}$. For the parameter of $\theta_{ave,\theta < \theta_c}$, since we did not measure the average misorientation angle experimentally, the average angle was assumed to be a median within the range of misorientation angles considered. Thus, for θ_c of 2 deg, 5 deg, 10 deg, and 15 deg, $\theta_{ave,\theta < \theta_c}$ was set as 1 deg, 2.5 deg, 5 deg, and 7.5 deg, respectively.

The calculated yield stress for the as-deformed samples is shown in Figure 9, where the strength contribution from friction stress, dislocation strengthening, and grain boundary strengthening are indicated as bar graph in white, red, and green, respectively. When the critical angle is set at 0 deg (Figure 9(a)), which considers that all boundaries including dislocation cell boundaries, sub-grain boundaries, and high-angle boundaries act as conventional grain boundaries, the calculated yield stress is underestimated compared to the experimentally determined yield stress. On the other hand, the critical angle of 5 deg and above gives an overestimation (Figures 9(c) and (d)). In this figure, the result of the critical angle of 15 deg is not shown, but the calculation is much larger than the experiment as well. It is seen that

the calculation using the critical angle of 2 deg is in good agreement with the experiment (Figure 9(b)). This tendency corresponds well with the previous reports.[10] This analysis suggests that in the as-deformed state, low-angle dislocation boundaries with misorientation angles of 2 deg and above act as conventional grain boundaries for dislocation glide, while very low-angle dislocation boundaries with misorientation angles below 2 deg act as forest dislocations for dislocation glide. In other words, it is suggested that boundaries with misorientation angles of 2 deg and above are strong enough as obstacles for dislocation glide.

Since the calculated strength in Figure 9(b), using the critical angle of 2 deg, can reasonably reproduce the experimental tendency, the observed deformation-induced decrease in yield stress can basically be understood by the balance of dislocation strengthening and grain boundary strengthening. Table III summarizes the structural parameters and each strength contribution to obtain Figure 9(b). σ_{gb} increases with increasing the strain up to CR90 + 3c ARB sample, but it tends to be saturated by further deformation, reflecting the change in $d_{R,\theta > 2 \text{ deg}}$. On the other hand, in terms of the change in dislocation strengthening, σ_{dis} increases with increasing the strain, but it reaches a maximum in CR90 sample, and then decreases significantly from CR90 sample to CR90 + 5c ARB sample. Thus, the deformation-induced softening observed in high strain is mainly due to a decrease in dislocation strengthening. It should be noted that $\rho_{\theta < 2 \text{ deg}}$ is much higher than ρ_0, indicating that the density of dislocations stored in low-angle dislocation boundaries is more dominant to determine the dislocation strengthening than that of

Table III. Structural Parameters Used for Strength Calculation at a Critical Angle of 2 Deg for the As-deformed Samples

Sample Names	ε_{eq}	$\sigma_{0.2,exp}$ (MPa)	$\sigma_{0.2,cal}$ (MPa)	σ_0 (MPa)	σ_{dis} (MPa)	σ_{gb} (MPa)	ρ_0 (m^{-2})	$\rho_{\theta < 2\,deg}$ (m^{-2})	ρ_{total} (m^{-2})	$d_{R,\theta > 2\,deg}$ (μm)
Undeformed	0	19.0	12.9	9.7	0	3.2	not measured	not measured	not measured	162
CR50	0.8	94.0	104	9.7	70.2	23.9	0.097×10^{14}	1.6×10^{14}	1.7×10^{14}	2.9
CR90	2.7	120	137	9.7	92.6	35.2	0.44×10^{14}	2.4×10^{14}	2.9×10^{14}	1.4
CR90 + 3c ARB	5.1	118	125	9.7	70.6	44.3	0.21×10^{14}	1.5×10^{14}	1.7×10^{14}	0.86
CR90 + 5c ARB	6.7	108	102	9.7	44.7	47.2	0.27×10^{14}	0.40×10^{14}	0.67×10^{14}	0.76
CR90 + 7c ARB	8.3	105	100	9.7	44.7	45.3	0.17×10^{14}	0.50×10^{14}	0.67×10^{14}	0.82

individual dislocations between the boundaries. It can therefore be concluded from the above analysis that the observed deformation-induced softening in high strain is mainly due to the significant decrease in the density of low-angle dislocation boundaries with misorientation angles below 2 deg.

B. Strengthening Mechanisms of Ultrafine-grained and Sub-grained Metals

A similar strength calculation using Eq. [9] is also applied to the annealed samples to understand the strengthening mechanisms of nanostructured metals. It is assumed that the distribution of boundary misorientation angles does not change significantly from the as-deformed to annealed state in samples of CR50, CR90, and CR90 + 3c ARB that reveal slight sub-grain coarsening during annealing (Figure 3), and that the fraction of boundaries with different misorientation angles in the annealed samples is the same as in the as-deformed samples. It is also assumed that for all annealed samples individual dislocations between the boundaries have been annealed out, and ρ_0 is considered to be zero. Based on the analysis in the as-deformed samples in Figure 9, the critical angle of 2 deg to separate dislocation strengthening from grain boundary strengthening is considered to be reasonable even for the calculation in the annealed samples. Figure 10 shows the comparison between the experimentally obtained and calculated yield stress for selected annealed samples.

For the CR50, CR90, and CR90 + 3c ARB samples (Figures 10(a) through (c)), the calculated strength is relatively good agreement with the experimental strength. Thus, it is found that the yield stress can basically be understood by a balance of dislocation strengthening and grain boundary strengthening for sub-grained samples dominated by low-angle boundaries. On the other hand, different tendencies can be seen for the CR90 + 5c ARB + annealed samples (Figure 10(d)). Good agreement between the experiment and calculation can be observed for both as-deformed and coarse-grained sample with the average grain size of 17 μm. However, for the well-annealed ultrafine-grained samples with the average boundary spacing of 1.6 and 3.2 μm, the calculation is underestimated, corresponding well with the previous work.[10] It should be emphasized that these well-annealed ultrafine-grained samples are those who reveal unusual discontinuous yielding in tensile test (see Figure 7(d)). Thus, such a discrepancy between the calculation and experiment is
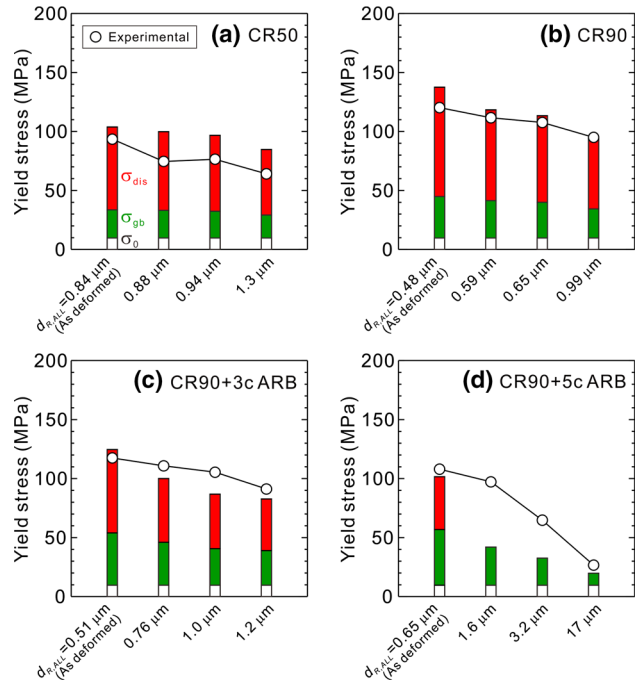

Fig. 10—Structure-based yield stress calculation for deformed and annealed samples, assuming that strengthening contributions from dislocations and grain boundaries are simply additive. The critical angle to separate between dislocation boundaries and grain boundaries is set as 2 deg. (a) CR50, (b) CR90, (c) CR90 + 3c ARB, and (d) CR90 + 5c ARB samples.

attributed to the occurrence of discontinuous yielding and resultant extra Hall–Petch strengthening.

The above strength calculation reveals that the yield stress of as-deformed and sub-grained samples that show continuous yielding can reasonably be explained by the sum of dislocation strengthening and grain boundary strengthening, where the Hall–Petch coefficient for coarse grains (41 MPa μm$^{1/2}$) was used to calculate grain boundary strengthening. This indicates that the observed extra Hall–Petch strengthening in the as-deformed and sub-grained samples is just an apparent behavior, and the mechanism of grain boundary strengthening in these samples should be identical to that in coarse-grained samples. On the other hand, for the well-annealed ultrafine-grained samples that show discontinuous yielding, the calculated yield stress is much lower than the experimental yield stress, when the Hall–Petch coefficient of 41 MPa μm$^{1/2}$ was used, indicating that the observed extra Hall–Petch strengthening

is a true behavior. It is suggested that the mechanism of grain boundary strengthening in discontinuous yielding is different from that in continuous yielding, and the former is much more significant than the latter, leading to an increased Hall–Petch coefficient in the well-annealed ultrafine-grained samples.

The unusual discontinuous yielding observed in well-annealed ultrafine-grained pure aluminum can be understood in the following way. In general, it has been well established that one important criterion to reveal discontinuous yielding is a lack of mobile dislocations in the crystals.[57–59] In well-annealed ultrafine-grained structures, two reasons might be responsible for the lack of mobile dislocations. Firstly, since ultrafine-grained structures are composed of narrowly spaced high-angle grain boundaries, these boundaries may act as sinks for dislocations,[21,60–62] leading to enhanced recovery of dislocations at the boundaries during annealing. Thus, the density of mobile dislocations that act as dislocation sources might be quite low. Secondly, even dislocation sources are present in ultrafine-grained structures, such dislocation sources might be difficult to nucleate and propagate. Possible dislocation sources could be Frank–Read dislocation sources within ultrafine grains[22,23] or grain boundary dislocation sources.[24–27] In both cases, it is considered that the length of dislocation sources significantly decreases when the grain size decreases down to the micrometer or sub-micrometer-scale, so an extremely high stress should be required to activate such dislocation sources in ultrafine-grained metals. For these two reasons, the density of mobile dislocations that act as easy dislocation sources may be quite low. In that situation, a very high stress is required to activate dislocation sources or nucleate new dislocation sources, leading to a localized shear, *i.e.*, Lüders deformation, in the shoulder part, resulting in the occurrence of discontinuous yielding in the well-annealed ultrafine-grained samples.

On the other hand, the as-deformed ultrafine-grained samples, sub-grained samples, and coarse-grained samples show continuous yielding. The reason for the occurrence of continuous yielding in these samples could be that these samples have enough dislocation sources that can easily be activated in the structure. In the as-deformed ultrafine-grained samples, a large number of individual dislocations should still be present in the structure, and such dislocations may act as easy dislocation sources for plastic deformation. In the case of sub-grained samples, dislocations in low-angle boundaries may act as easy dislocation sources,[61–63] leading to a lower yield stress to plastically deform, compared with the well-annealed ultrafine-grained samples. In the coarse-grained samples, since a volume of grain is quite large, Frank–Read dislocation sources within the grains would be activated very easily at a low stress, where the stress required to activate dislocation sources may not be so sensitive to the boundary misorientation. This might be the reason why the yield stress can be explained by a single Hall–Petch curve, regardless of the boundary misorientation angles in coarse grains.

Based on the observations and discussion above, the following conclusions can be obtained. When the samples have enough dislocation sources that can easily be activated in the structure, yielding behavior should be continuous. In this situation, the yield stress can be understood by a sum of dislocation strengthening and conventional grain boundary strengthening using the Hall–Petch coefficient in coarse grains. On the other hand, in the well-annealed ultrafine-grained samples, due to the lack of mobile dislocations and the strengthening of dislocation sources, the grain boundary strengthening is significantly enhanced, leading to an increase in the Hall–Petch coefficient.

V. CONCLUSIONS

In this study, tensile behavior of ultrafine-grained and sub-grained aluminum was systematically investigated, and the correlation between microstructures and mechanical properties was discussed in detail. The obtained results are summarized as follows:

(1) Well-annealed ultrafine-grained samples dominated by high-angle boundaries, with the average grain size of 1 to 10 μm, showed unusual discontinuous yielding, leading to extra Hall–Petch strengthening. This should be due to the lack of mobile dislocations and the strengthening of dislocation sources.

(2) Yielding behavior of as-deformed ultrafine-grained samples was continuous. It is suggested that individual dislocations present in the structure may act as dislocation sources, leading to a lower yield stress and continuous yielding.

(3) Sub-grained samples dominated by low-angle dislocation boundaries revealed continuous yielding. In the case of sub-grained samples, dislocations stored in the low-angle dislocation boundaries may act as dislocation sources, leading to easy yielding.

(4) In the as-deformed and sub-grained samples that have enough dislocation sources in the structure, the mechanism of grain boundary strengthening would be identical to that in coarse grains. In the well-annealed ultrafine-grained samples, grain boundary strengthening is significantly enhanced due to the lack of easy dislocation sources, leading to an increase in the Hall–Petch coefficient.

(5) Low-angle dislocation boundaries with misorientation angles of 2 deg and above may act as conventional grain boundaries for dislocation glide and contribute to the strength as the Hall–Petch strengthening.

REFERENCES

1. E.O. Hall: *Proc. Phys. Soc. B*, 1951, vol. 64, pp. 747–53.
2. N.J. Petch: *J. Iron Steel Inst.*, 1953, vol. 174, pp. 25–28.
3. L.L. Shaw: *J. Met.*, 2000, vol. 52, pp. 41–45.
4. R.Z. Valiev, Y. Estrin, Z. Horita, T.G. Langdon, M.J. Zechetbauer, and Y.T. Zhu: *J. Met.*, 2006, vol. 58, pp. 33–39.
5. A. Azushima, R. Kopp, A. Korhonen, D.Y. Yang, F. Micari, G.D. Lahoti, P. Groche, J. Yanagimoto, N. Tsuji, A. Rosochowski, and A. Yanagida: *CIRP Ann. Manuf. Technol.*, 2008, vol. 57, pp. 716–35.
6. M.A. Meyers, A. Mishra, and D.J. Benson: *Prog. Mater. Sci.*, 2006, vol. 51, pp. 427–556.
7. R.Z. Valiev, A.P. Zhilyaev, and T.G. Langdon: *Bulk Nanostructured Materials: Fundamentrals and Applications*, Wiley, Hoboken, NJ, 2014.
8. R.Z. Valiev and Y. Zhu: *Trans. Mater. Res. Soc. Jpn*, 2015, vol. 40, pp. 309–18.
9. C.Y. Yu, P.W. Kao, and C.P. Cheng: *Acta Mater.*, 2005, vol. 53, pp. 4019–28.
10. N. Kamikawa, X. Huang, N. Tsuji, and N. Hansen: *Acta Mater.*, 2009, vol. 57, pp. 4198–4208.
11. G.M. Le, A. Godfrey, and N. Hansen: *Mater. Des.*, 2013, vol. 49, pp. 360–67.
12. K.N. Zhu, A. Godfrey, N. Hansen, and X.D. Zhang: *Mater. Des.*, 2017, vol. 117, pp. 95–103.
13. S. Gao, M. Chen, S. Chen, N. Kamikawa, A. Shibata, and N. Tsuji: *Mater. Trans.*, 2014, vol. 55, pp. 73–77.
14. S. Gao, M. Chen, M. Joshi, A. Shibata, and N. Tsuji: *J. Mater. Sci.*, 2014, vol. 49, pp. 6536–42.
15. J.W. Wyrzykowski and M.W. Grabski: *Mater. Sci. Eng.*, 1982, vol. 56, pp. 197–200.
16. Y.Z. Tian, S. Gao, L.J. Zhao, S. Lu, R. Pippan, Z.F. Zhang, and N. Tsuji: *Scripta Mater.*, 2018, vol. 142, pp. 88–91.
17. D. Terada, M. Inoue, H. Kitahara, and N. Tsuji: *Mater. Trans.*, 2008, vol. 49, pp. 41–46.
18. Z. Li, L. Fu, and A. Shan: *Mater. Lett.*, 2013, vol. 96, pp. 1–4.
19. N. Tsuji, Y. Ito, Y. Saito, and Y. Minamino: *Scripta Mater.*, 2002, vol. 47, pp. 893–99.
20. R. Saha, R. Ueji, and N. Tsuji: *Scripta Mater.*, 2013, vol. 68, pp. 813–16.
21. X. Huang, N. Tsuji, and N. Hansen: *Science*, 2006, vol. 312, pp. 249–51.
22. T. Ohashi, M. Kawamukai, and H.M. Zbib: *Int. J. Plast.*, 2007, vol. 23, pp. 897–914.
23. Y. Aoyagi, T. Tsuru, and T. Shimokawa: *Int. J. Plast.*, 2014, vol. 55, pp. 43–57.
24. S. Cheng, J.A. Spencer, and W.W. Milligan: *Acta Mater.*, 2003, vol. 51, pp. 4505–18.
25. M. Kato, T. Fujii, and S. Onaka: *Mater. Trans.*, 2008, vol. 49, pp. 1278–83.
26. I.A. Ovid'ko and N.V. Skiba: *Scripta Mater.*, 2012, vol. 67, pp. 13–16.
27. I.A. Ovid'ko, A.G. Sheinerman, and R.Z. Valiev: *Scripta Mater.*, 2014, vol. 76, pp. 45–48.
28. H. Van Swygenhoven, M. Spaczér, and A. Caro: *Nanostruct. Mater.*, 1998, vol. 10, pp. 819–28.
29. H. Van Swygenhoven, M. Spaczér, D. Farkas, and A. Caro: *Nanostruct. Mater.*, 1999, vol. 12, pp. 323–26.
30. K. Kinoshita, T. Shimokawa, and T. Kinari: *Mater. Trans.*, 2012, vol. 53, pp. 147–55.
31. J.W. Wyrzykowski and M.W. Grabski: *Philos. Mag. A*, 1986, vol. 53, pp. 505–20.
32. P.L. Sun, C.Y. Yu, P.W. Kao, and C.P. Chang: *Scripta Mater.*, 2005, vol. 52, pp. 265–69.
33. N. Kamikawa, T. Hirochi, and T. Furuhara: *Proc. 33rd Risø Int. Symp. Mater. Sci. Nanomet. Status Perspect.*, Technical University of Denmark, 2012, pp. 257–64.
34. T. Hu, K. Ma, T.D. Topping, B. Saller, A. Yousefiani, J.M. Schoenung, and E.J. Lavernia: *Scripta Mater.*, 2014, vols. 78–79, pp. 25–28.
35. V.V. Polyakova, I.P. Semenova, A.V. Polyakov, D.K. Magomedova, Y. Huang, and T.G. Langdon: *Mater. Lett.*, 2017, vol. 190, pp. 256–59.
36. J.R. Gatti and P.P. Bhattacharjee: *J. Alloys Compds*, 2014, vol. 615, pp. 950–61.
37. I. Zuiko and R. Kaibyshev: *Mater. Sci. Eng. A*, 2017, vol. 702, pp. 53–64.
38. T. Huang, L. Shuai, A. Wakeel, G. Wu, N. Hansen, and X. Huang: *Acta Mater.*, 2018, vol. 156, pp. 369–78.
39. Y. Saito, H. Utsunomiya, N. Tsuji, and T. Sakai: *Acta Mater.*, 1999, vol. 47, pp. 579–83.
40. L. Su, C. Lu, H. Li, G. Deng, and K. Tieu: *Mater. Sci. Eng. A*, 2014, vol. 614, pp. 148–55.
41. Y.B. Zhang and O.V. Mishin: *Mater. Charact.*, 2017, vol. 129, pp. 323–28.
42. N. Kamikawa, N. Tsuji, X. Huang, and N. Hansen: *Acta Mater.*, 2006, vol. 54, pp. 3055–66.
43. R.K. Ham: *Philos. Mag.*, 1961, vol. 6, pp. 1183–84.
44. N. Kamikawa and N. Tsuji: *Mater. Trans.*, 2016, vol. 57, pp. 1720–28.
45. Y. Ito and Z. Horita: *Mater. Sci. Eng. A*, 2009, vol. 503, pp. 32–36.
46. N. Kamikawa and T. Furuhara: *J. Mater. Process. Technol.*, 2013, vol. 213, pp. 1412–18.
47. Y. Ito, K. Edalati, and Z. Horita: *Mater. Sci. Eng. A*, 2017, vol. 679, pp. 428–34.
48. Z. Horita, K. Kishikawa, K. Kimura, K. Tatsumi, and T.G. Langdon: *Mater. Sci. Forum*, 2007, vols. 558–559, pp. 1273–78.
49. R.Z. Valiev, I.V. Alexandrov, Y.T. Zhu, and T.C. Lowe: *J. Mater. Res.*, 2002, vol. 17, pp. 5–8.
50. H.W. Höppel, J. May, and M. Göken: *Adv. Eng. Mater.*, 2004, vol. 6, pp. 781–84.
51. H.-W. Kim, S.-B. Kang, N. Tsuji, and Y. Minamino: *Acta Mater.*, 2005, vol. 53, pp. 1737–49.
52. J.E. Bailey and P.B. Hirsch: *Philos. Mag.*, 1960, vol. 5, pp. 485–97.
53. N. Hansen: *Scripta Mater.*, 2004, vol. 51, pp. 801–06.
54. N. Hansen and X. Huang: *Acta Mater.*, 1998, vol. 46, pp. 1827–36.
55. G.W.C. Kaye and T.H. Laby: *Tables of Physical and Chemical Constants*, 14th ed., Longman, London, 1973, p. 31.
56. G.I. Taylor: *J. Inst. Met.*, 1938, vol. 62, pp. 307–24.
57. W.G. Johnston: *J. Appl. Phys.*, 1962, vol. 33, pp. 2716–30.
58. E.O. Hall: *Yield Point Phenomena in Metals and Alloys*, Plenum Press, New York, 1970.
59. D.J. Lloyd: *Met. Sci.*, 1980, vol. 14, pp. 193–98.
60. M.W. Grabski and R. Korski: *Phil. Mag.*, 1970, vol. 22, pp. 707–715.
61. J.P. Hirth: *Metall. Trans.*, 1972, vol. 3, pp. 3047–67.
62. J. Kacher, B.P. Eftink, B. Cui, and I.M. Robertson: *Curr. Opin. Solid State Mater. Sci.*, 2014, vol. 18, pp. 227–43.
63. J.C.M. Li: *Trans. Metall. Soc. AIME*, 1963, vol. 227, pp. 239–47.